

Debond Analyses for Stitched Composite Structures

E.H. Glaessgen
National Research Council
Hampton, VA 23681, U.S.A.

I.S. Raju and C.C. Poe, Jr.
NASA Langley Research Center
Hampton, VA 23681, U.S.A.

Summary

The effect of stitching on mode I and mode II strain energy release rates for debond configurations is studied using an analysis based on plate finite elements and the virtual crack closure technique. The stitches were modeled as discrete nonlinear fastener elements with a compliance determined by experiment. The axial and shear behavior of the stitches was considered with both the compliances and failure loads assumed to be independent. The mode I strain energy release rate, G_I , was shown to decrease once the debond had grown beyond the first row of stitches and was reduced to zero for long debonds, however, the mode II strain energy release rate, G_{II} , continued to be of significant magnitude over the range of debond lengths considered.

Introduction

Warp-knit carbon/epoxy textile composite materials are currently being considered for use in primary aircraft structures. Stitching the stiffeners to the skin is expected to suppress the initiation and growth of debonds between the stiffeners and skin. The structural skins are typically made of between two and ten stacks (layers of woven material) of 1.40 mm. thick carbon warp-knit fabric that is layered and stitched with Kevlar yarns. The stiffeners and intercostals are fabricated with a similar number of stacks of stitched fabric and are stitched to the skin. Once the preform is assembled, resin film infusion (RFI) is used to impregnate the entire structure with epoxy resin [1].

Skin-stiffener interface stresses may be large enough to cause a separation between the skin and stiffening elements resulting in a delamination or debond [2]. The effects of stitching on delamination or debond growth in composites have been examined in simple two- and three-dimensional configurations by modeling the stitches as truss or beam elements connecting nodes through the thickness of the material [3-5]. An advantage of the three-dimensional modeling is to allow the stitches to be modeled discretely rather than as structural components with an “effective” stiffness. References 2,6,7 proposed the use of plate elements to model skin-stiffener debond problems and calculate strain energy release rates using the virtual crack closure technique (VCCT). The approach taken in references 2,6-8 and the present analysis, is to place the skin nodes and the stiffener nodes along the interface between the skin and the stiffener. The positioning of these nodes at the interface is performed by defining an offset distance from the mid-plane of both the skin and the stiffener.

The objective of this paper is to quantify the effect of stitches on the mode I and mode II strain energy release rates of the mixed mode skin-stiffener debond configuration shown in Figure 1. The plate element modeling technique is used to analyze the debond configurations and the VCCT is used to calculate strain energy release rates. Because the skin nodes and corresponding stiffener nodes are coincident in the bonded region, the plate element models do not allow for nodal connectivity beyond the element interface. Thus, the stitches are not modeled as finite length spar or beam elements as in references 3-5, but rather as nonlinear fastener elements with axial and shear compliances determined by experiment. In this paper, the stitched skin-stiffener configuration is analyzed and the strain energy release rates and stitch forces are evaluated for various debond lengths.

Analysis

Considerable insight into the behavior of complicated debond configurations can be gained by examining simple configurations such as the flange-skin configuration shown in Figure 1 while reducing

modeling complexity. The configuration was modeled as an infinitely wide strip of length $L_1=L_2=2.54$ cm. with a skin and stiffener flange of equal thickness, t , of 0.56 cm. and subjected to cylindrical bending repeating unit boundary conditions ($v=0$, $\theta_x=0$ on $y=\pm s_y/2$ in Figure 1).

Material and skin thicknesses that are representative of the stitched composite wing skin used in a NASA program are considered [1]. The same material is assumed for both the skin and the stiffener flange with each stack of material oriented with its primary axis in the x -direction. The equivalent laminate stacking sequence is $(45/-45/0/90/0/-45/45)_{ns}$ with areal weights of $1.73\text{E-}4$ N/cm², $3.62\text{E-}4$ N/cm² and $1.95\text{E-}4$ N/cm² for the forty-five, zero and ninety degree plies, respectively. In these analyses, the laminates are assumed to be homogeneous with properties

$$\begin{aligned} E_{11} &= 63.8 \text{ GPa} & \mu_{12} &= \mu_{13} = 15.7 \text{ GPa} & \nu_{12} &= \nu_{13} = 0.397 \\ E_{22} &= E_{33} = 32.2 \text{ GPa} & \mu_{23} &= 3.43 \text{ GPa} & \nu_{23} &= 0.490 \end{aligned}$$

where E_{ij} , μ_{ij} , ν_{ij} ($i,j=1,2,3$) are the Young's moduli, shear moduli, and Poisson's ratio, respectively, and the subscripts 1,2,3 represent the fiber and two transverse directions, respectively. The stitch spacings, s_x and s_y , were assumed to be 3.18 mm. in the x - and y -directions, respectively (see Figure 1).

The STAGS 480, 9-node quadratic shear deformable, plate/shell element [9] is used for modeling the debond configurations. A representation of the 9-noded plate elements near a debond front with rectangular grid type modeling is shown in Figure 2. The element size chosen was 0.13 mm. in the x -direction by 0.80 mm. in the y -direction as shown in Figure 1. The virtual crack closure technique (VCCT) [10,11] can be used to calculate strain energy release rates, G , with plate elements using the techniques discussed in references 2,6-8. Reference 8 suggests that allowing the elements ahead of the debond front to have independent (free) rotations ensures accurate evaluation of the strain energy release rates. With this assumption, the G values can be calculated using the nodal forces (F_x , F_y , F_z) and displacements (u , v , w) near the debond front as (see Figure 2) [6]

Mode-I components:

$$\begin{aligned} (G_I)_i &= -\frac{1}{2\Delta b_i} \left[F_{z_i} (w_p - w_{p'}) + F_{z_e} (w_l - w_{l'}) \right] \\ (G_I)_j &= -\frac{1}{2\Delta b_j} \left[F_{z_j} (w_q - w_{q'}) + F_{z_f} (w_m - w_{m'}) \right] \\ (G_I)_k &= -\frac{1}{2\Delta b_k} \left[F_{z_k} (w_r - w_{r'}) + F_{z_g} (w_n - w_{n'}) \right] \end{aligned} \tag{1}$$

Mode-II components:

$$\begin{aligned} (G_{II})_i &= -\frac{1}{2\Delta b_i} \left[F_{x_i} (u_p - u_{p'}) + F_{x_e} (u_l - u_{l'}) \right] \\ (G_{II})_j &= -\frac{1}{2\Delta b_j} \left[F_{x_j} (u_q - u_{q'}) + F_{x_f} (u_m - u_{m'}) \right] \\ (G_{II})_k &= -\frac{1}{2\Delta b_k} \left[F_{x_k} (u_r - u_{r'}) + F_{x_g} (u_n - u_{n'}) \right] \end{aligned} \tag{2}$$

Mode III components can be calculated in a similar manner using y -forces and relative v -displacements. However, mode III components are negligible for this configuration and are identically zero at locations corresponding to $y=-s_y/2$, 0 and $s_y/2$ (Figure 1) due to local symmetry and hence are not reported here.

Equations (1) and (2) assume that the elements have the same length, Δ , ahead of and behind the debond front. The equivalent widths apportioned to the two corner debond-front nodes are b_i and b_k , and to the midside debond-front node is b_j and are taken as

$$b_i = \frac{1}{6}[b_{J-1} + b_J], b_j = \frac{2}{3}b_J, b_k = \frac{1}{6}[b_J + b_{J+1}], \quad (3)$$

where b_{J-1} , b_J and b_{J+1} are the widths of layers $J-1$, J and $J+1$, respectively, as shown in Figure 2(b).

The strain energy release rates along the debond front of the mixed-mode skin-stiffener debond configurations are calculated using equations (1)-(3). The configurations have been analyzed with a geometrically nonlinear finite element analysis using the STAGS finite element code.

Closure of the debond faces may occur once the debond is of sufficient length. In the finite element analysis, contact of the faces is allowed, while interpenetration of the faces is not. Interpenetration of the faces can be prevented either by adding gap elements (STAGS 810 PAD elements) to the model between the debond faces where interpenetration is likely to occur or by adding multipoint constraints along a known region of interpenetration to impose the requirement of identical z -direction displacements among elements in contact. No constraint on the relative sliding displacements (u) is imposed using either technique. The latter procedure was used in the present analysis although it requires that multiple analyses be executed to determine the actual contact length.

The fastener elements used in this analysis are imposed as nonlinear constraints within the plate element model [9]. These fastener elements have both an axial and a shear stiffness, K_{axial} and K_{shear} , respectively. Only the fastener elements behind the debond front ($L_1 < x < L_1 + a$ in Figure 1) carry load since the upper and lower plate elements ahead of the debond front are coupled using constraint equations to have identical translational displacements. Accurate compliance curves for both axial and shear behavior of the stitches were developed in reference 12 using flatwise tension and double lap shear tests, respectively. A piecewise linear representation of this data is used in the finite element model with failure occurring at 258 N in tension and 169 N in shear. For the purposes of this analysis, the axial and shear responses of the stitches are assumed to be independent.

Results and Discussion

The mixed-mode skin-stiffener debond configuration assumes self-similar debond growth between the skin and stiffener. Thus, no variation in G across the width of the model is assumed and the values of G reported are those calculated along the lines of the stitching ($y=0$ in Figure 1). Examination of the distribution of G_I and G_{II} across the width for this debond configuration shown in Figure 1 showed less than two percent difference between the location in line with the stitches ($y=0$) and the location midway between the stitches ($y=\pm s_y/2$, see Figure 1).

The skin-stiffener debond configuration exhibits both mode I and mode II deformations at the debond front. As shown in Figure 3(a), for a fixed applied load, p , of 226 kN/m, both the mode I and mode II strain energy release rates, G_I and G_{II} , respectively, for the unstitched configurations increase with increasing debond length over the range of debond lengths, a , considered. Stitching significantly affects both G_I and G_{II} . G_I initially increases with debond length and then begins to decrease after the debond passes the first stitch (first vertical line in Figure 3a), decreasing as additional stitches begin to carry load, eventually reaching values of zero for long debonds ($a/t > 2.3$). These zero values for long debonds correspond to a region of contact immediately behind the debond front that increases with increasing debond length. In contrast, G_{II} is a weak function of debond length and remains within 20% of its maximum value over the range considered. Thus, even though G_I is significantly reduced, there may be sufficient G_{II} present to grow the debond.

Figures 3(b) and 3(c) show the axial and shear force in the stitches normalized by the force required for axial and shear failure, respectively. As seen in Figure 3(b), only stitches 1 through 3 have nonzero axial force (F_{axial}) over the range of debond lengths considered. The axial force reaches a near-constant value for debond lengths corresponding to the region of zero G_I ($a/t > 2.3$). However, a shearing force (F_{shear}), shown in Figure

3(c), is also present in the stitches and is nonzero for all of the stitches (stitches 1 through 6) along the debond. Results were evaluated from the finite element model with increments of debond growth of 0.32 cm. ($a/t=0.57$), so the force corresponding to the first 0.32 cm. ($a/t=0.57$) of debond growth beyond a given stitch location in the finite element model was not recovered in the analysis and is represented by the dashed lines in the figure. For the longest debond considered in this analysis ($a/t=4.6$) corresponding to 80% of L_1+a in Figure 1, the normalized shear force ($F_{shear}/F_{shear failure}$) in the first stitch is larger than the corresponding normalized axial force ($F_{axial}/F_{axial failure}$). There are two ways that the debond may continue to grow in this mixed-mode configuration. If the stitches remain intact, the debond may continue to grow by mode II as shown in Figure 3(a). However, if the stitches fail, non-zero mode I may be present and may also contribute to the growth of the debond. The present analysis suggests that the former may be the preferred growth mode for this configuration.

Concluding Remarks

The effect of stitching on mode I and mode II strain energy release rates for debond configurations was studied using an analysis based on plate finite elements and the virtual crack closure technique. The plate element modeling technique was used to model the configuration and the virtual crack closure technique (VCCT) was used to calculate the strain energy release rates. The debond growth between the flange and the skin was shown to be approximately self-similar and continuous along the length of the flange-skin interface. The stitches were modeled as discrete nonlinear fastener elements with their compliance determined by experiment. Both axial and shear behavior of the stitches was considered, however, the two compliances and failure loads were assumed to be independent.

The stitches began to carry considerable load and cause G_I to decrease once the debond length became sufficiently long. In contrast, the stitches had less effect on mode II and G_{II} remained significant throughout the range of debond lengths considered. Thus, there are two ways that the debond may continue to grow in this mixed-mode configuration. If the stitches do not fail, the debond may continue to grow by mode II, however if they do fail, the resulting mode I may also contribute to the growth of the debond.

References

1. Dow, M.B. and Dexter, H.B., "Development of Stitched, Braided and Woven Composite Structures in the ACT Program and at Langley Research Center," NASA TP-97-206234, November 1997.
2. Wang, J.T., Jegley, D.C., Bush, H.G. and Hinrichs, S.C., "Correlation of Structural Analysis and Test Results for the McDonnell Douglas Stitched/RFI All-Composite Wing Stub Box," NASA TM-110267, 1996.
3. Mignery, L.A., Tan, T.M., and Sun, C.T., "The Use of Stitching to Suppress Delamination in Laminated Composites," ASTM STP 876, 1985, pp. 371-385.
4. Sankar, B.V. and Sonik, V., "Modeling End-Notched Flexure Tests of Stitched Laminates," Proceedings of the American Society for Composites, ASC, 1995, pp. 172-181.
5. Lee, C. and Liu, D., "Tensile Strength of Stitching Joint in Woven Glass Fabrics," Journal of Engineering Materials and Technology, Vol. 112, April 1990, pp. 125-130.
6. Wang, J.T., Raju, I.S., and Sleight, D.W., "Composite Skin Stiffener Debond Analyses Using Fracture Mechanics Approach with Shell Elements," Composites Engineering, Vol. 5, No. 2, 1995, pp. 277-296.
7. Wang, J.T. and Raju, I.S., "Strain Energy Release Rate Formulae for Skin-Stiffener Debond Modeled with Plate Elements," Engineering Fracture Mechanics, Vol. 54, No. 2, 1996, pp. 211-228.
8. Glaessgen, E.H., Riddell, W.T. and Raju, I.S., "Effect of Shear Deformation and Continuity on Delamination Strain Energy Release Rate," 39th AIAA/ASME/ASCE/AHS Structures, Structural Dynamics and Materials Conference, AIAA Paper 98-2023, 1998.
9. Brogan, F.A., Rankin, C.C., Cabiness, H.D. and Loden, W.A., STAGS User Manual, Lockheed Martin Missiles and Space Co., July 1996.
10. Rybicki, E.F. and Kanninen, M.F., "A Finite Element Calculation of Stress Intensity Factors by a Modified Crack Closure Integral," Engineering Fracture Mechanics, Vol. 9, 1977, pp. 931-938.
11. Raju, I.S., "Calculation of Strain-Energy Release Rates with Higher Order and Singular Finite Elements," Engineering Fracture Mechanics, Vol. 28, No. 3, 1987, pp. 251-274.
12. Adams, D.O., "Stitch Compliance in Delaminated Composites," 29th SAMPE Technical Conference, Orlando, FL, October 28-31, 1997.

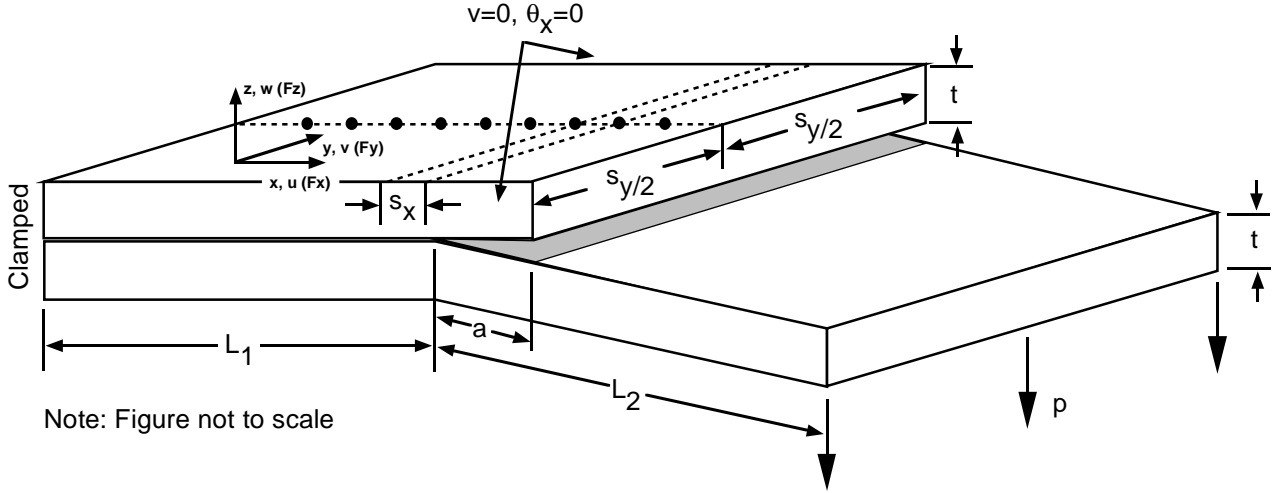
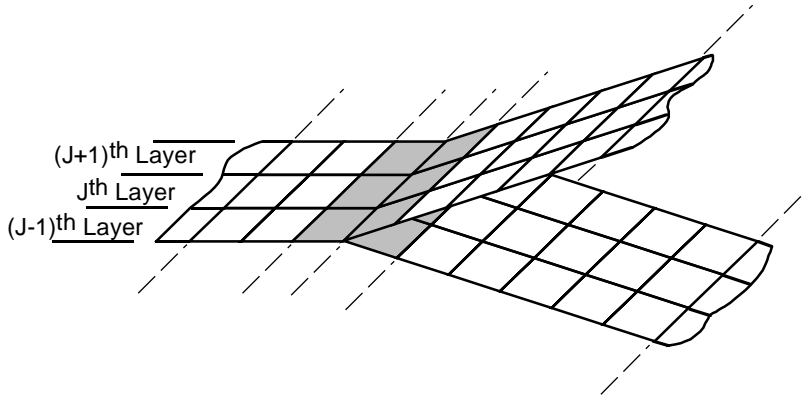
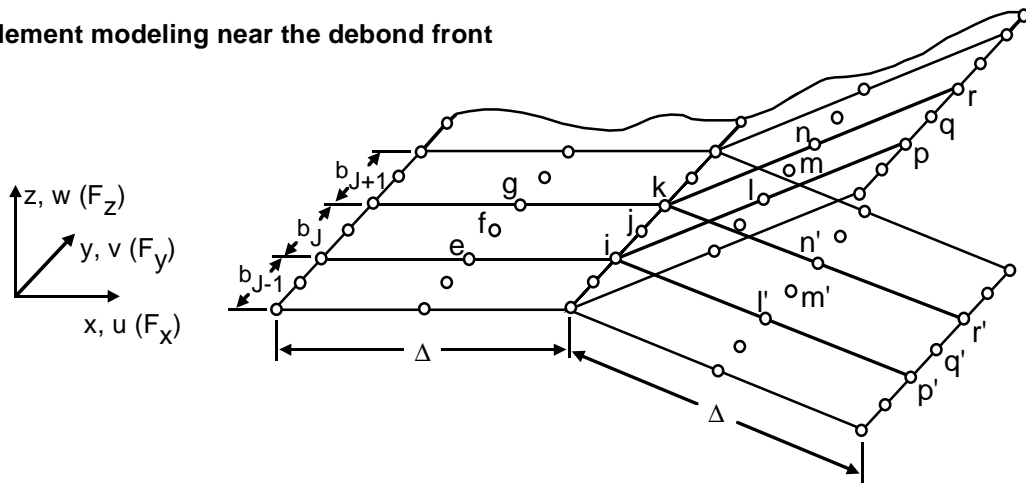


Figure 1 Mixed-mode debond configuration

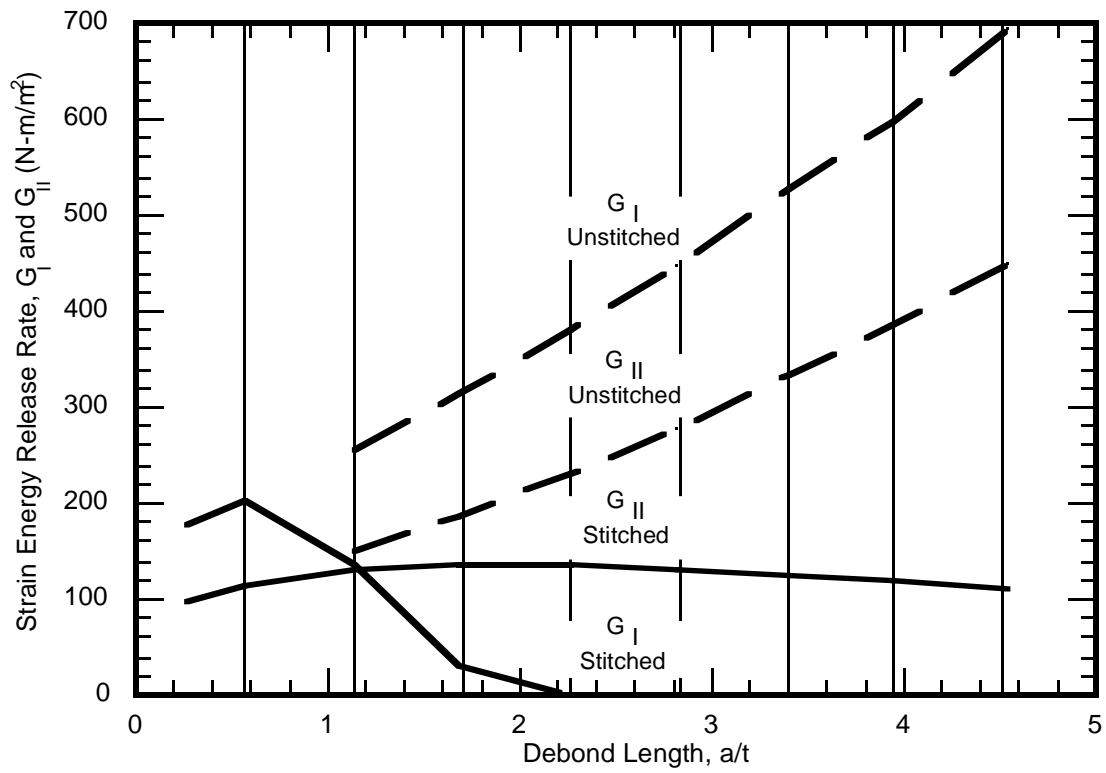


(a) Plate element modeling near the debond front

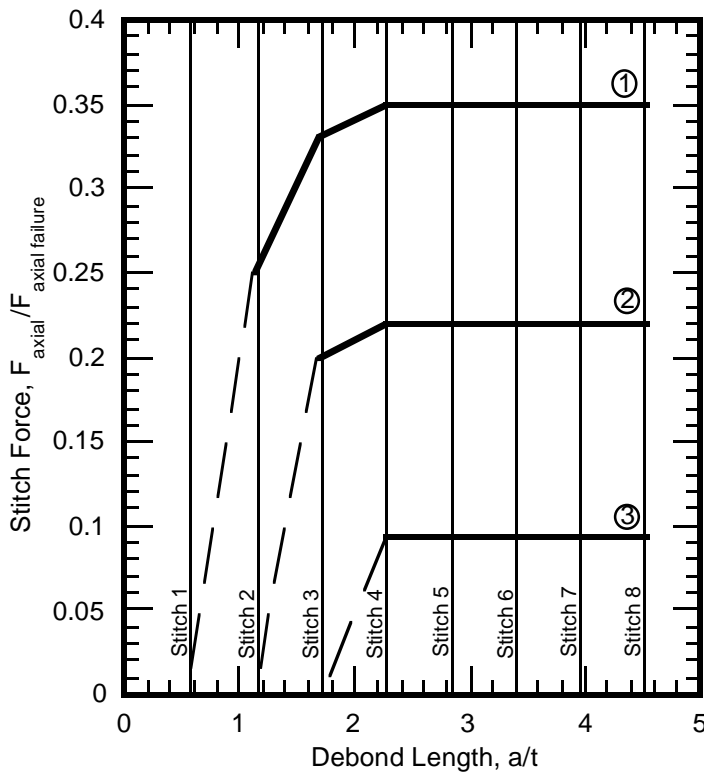


(b) Details of the model near the debond front

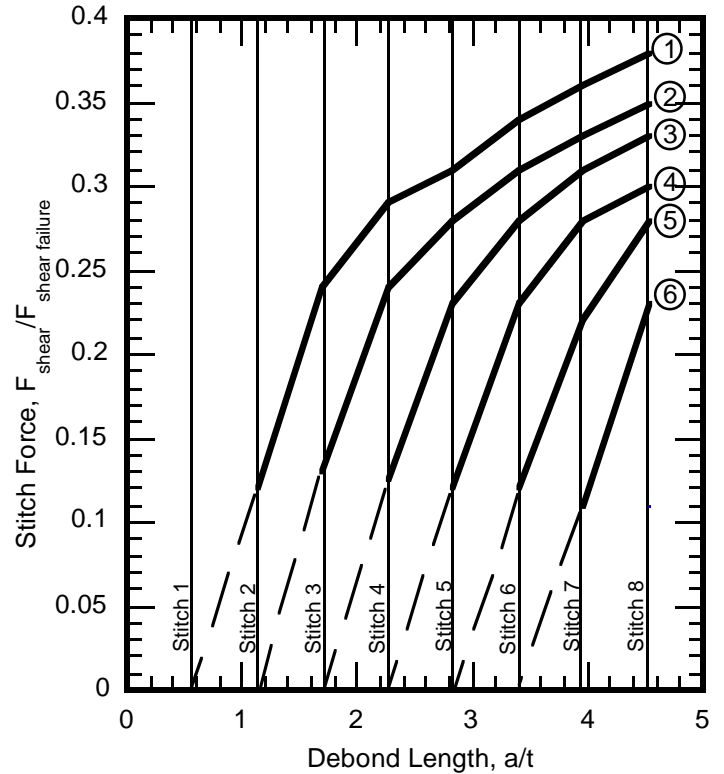
Figure 2 Debond configuration modeled using 9-node plate elements



(a) Strain energy release rate as a function of debond length



(b) Stitch shear force as a function of debond length



(c) Stitch axial force as a function of debond length

Figure 3 Effect of multiple stitches on G_I , G_{II} and stitch force
(Applied Load, $p=226 \text{ kN/m}$, $t=0.56 \text{ cm}$, $s_x=0.32 \text{ cm}$, $s_y=0.32 \text{ cm}$)